

Facile Microembossing Process for Microchannel Fabrication for Nanocellulose-Paper-Based Microfluidics

Wenwen Yuan, Hang Yuan, Keran Jiao, Jia Zhu, Eng Gee Lim,* Ivona Mitrovic, Sixuan Duan, Yongjie Wang, Shan Cong, Chun Zhao, Jie Sun, Xinyu Liu,* and Pengfei Song*



Cite This: <https://doi.org/10.1021/acsami.2c19354>



Read Online

ACCESS |

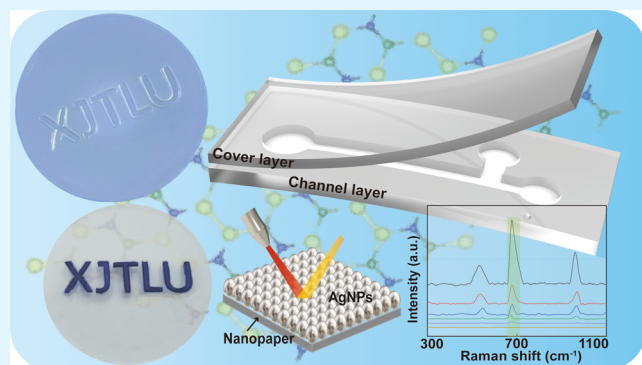
Metrics & More

Article Recommendations

Supporting Information

ABSTRACT: Nanofibrillated cellulose paper (nanopaper) has gained growing interest as one promising substrate material for paper-based microfluidics, thanks to its ultrasmooth surface, high optical transparency, uniform nanofiber matrix with nanoscale porosity, and tunable chemical properties. Recently, research on nanopaper-based microfluidics has quickly advanced; however, the current technique of patterning microchannels on nanopaper (i.e., 3D printing, spray coating, or manual cutting and sticking), that is fundamental for application development, still has some limitations, such as ease-of-contamination, and more importantly, only enabling millimeter-scale channels. This paper reports a facile process that leverages the simple operations of microembossing with the convenient plastic micro-molds, for the first time, patterning nanopaper microchannels downing to 200 μm , which is 4 times better than the existing methods and is time-saving (<45 mins). We also optimized the patterning parameters and provided one quick look-up table as the guideline for application developments. As proof-of-concept, we first demonstrated two fundamental microfluidic devices on nanopaper, the laminar-mixer and droplet generator, and two functional nanopaper-based analytical devices (NanoPADs) for glucose and Rhodamine B (RhB) sensing based on optical colorimetry and surface-enhanced Raman spectroscopy, respectively. The two NanoPADs showed outstanding performance with low limits of detection (2 mM for glucose and 19fM for RhB), which are 1.25 \times and 500 \times fold improvement compared to the previously reported values. This can be attributed to our newly developed highly accurate microchannel patterning process that enables high integration and fine-tunability of the NanoPADs along with the superior optical properties of nanopaper.

KEYWORDS: microembossing, nanocellulose-paper-based microfluidics, microchannel fabrication, functional nanopaper-based analytical devices, surface-enhanced Raman spectroscopy



INTRODUCTION

Recently, nanofibrillated cellulose (NFC) paper (nanopaper) has been emerging as one of the most promising substrate materials for many areas such as flexible electronics, energy devices, and biomedical, among others.^{1–4} Like regular cellulose paper, it is green, low-cost, biocompatible, and biodegradable, and can be obtained from natural plants.^{5,6} It also features many unique and important advantages. First, nanopaper has an ultrasmooth surface (less than 25 nm surface roughness) and a highly dense cellulose matrix structure.⁷ This feature is beneficial for building highly organized and uniform nanostructures that can facilitate the tunability and stability of nanopaper-based devices.^{8–10} This can be attributed to the abundant hydroxyl groups on the nanocellulose itself that promotes the tight and dense nanocellulose structure. Second, the nanopaper has high optical transparency and a low optical haze, and is an excellent substrate material for optical sensors.^{8,11,12} Third, the nanopaper also features the pump-

free flow. Though its dense structure does not allow the capillary driven flow within its cellulose matrix, the natural hydrophilicity also enables the autonomous flow at its surface. Thanks to the above advantages, nanocellulose has been widely used in various applications, including biomedical sensors,^{1,13} conductive electronic devices,^{12,14} cell culture platforms,^{9,15} supercapacitors, and batteries,^{12,16} among others. Nanocellulose is also naturally attractive for paper-based analytical microfluidic devices (μ PADs) as the new and promising substrate material, which could bring many unique properties that the regular chromatograph paper does not possess.

Received: October 27, 2022

Accepted: January 10, 2023

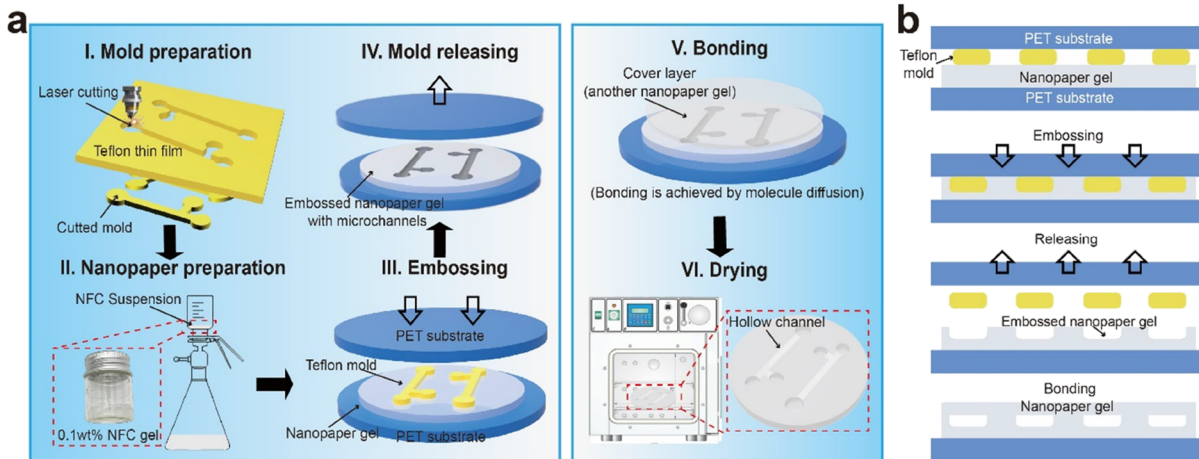


Figure 1. Schematic diagrams of the microembossing process for patterning microchannels on nanopaper. (a) Microembossing process consists of six steps: mold preparations, nanopaper filtration, embossing, mold releasing, bonding, and final drying. (b) Cross-sectional view of the microembossing process.

μ PADs have been extensively studied over the last decade, due to their cost-efficiency, biocompatibility, pump-free capability, and ease-of-fabrication,^{17,18} and have been demonstrated as the powerful point-of-care testing tools for disease screening in low-resource settings.^{19–21} One major breakthrough could be the invention of using wax printing for patterning microchannels on chromatography paper for developing functional μ PADs by George Whitesides Group²² and Bingcheng Lin Group.²³ After that, μ PADs have been quickly advanced, and many biosensing mechanisms such as enzyme-linked immunosorbent assay (ELISA),^{24–26} the electrochemical method,^{27,28} and chemiluminescence have been achieved on μ PADs for many types of biomarkers such as proteins,^{29,30} DNAs,^{31,32} RNAs,³³ and exosomes.³⁴ However, μ PADs still have some limitations, for instance, slow flow speeds, solvent evaporation, among others.

Several microchannel fabrication methods on nanopaper have been reported.^{9,35,36} The first reported nanopaper microchannel fabrication method relies on the 3D printing of sacrificial materials (trimethylchlorosilane) into nanopaper, forming hollow channels after removal. This sacrificial material creates a hydrophobic coating on the channel surface and thereby cannot achieve pump-free operation.³⁵ To tackle this problem, we have previously reported one method that uses a laser cutter to pattern the through channels on nanopaper, and then this channel layer is manually stacked between another two layers of nanopaper by ethylene vinyl acetate glue. This can realize liquid wick in hollow channels without any external pumping, but this method requires lots of manual operations.⁹ Another method builds microchannels through spray coating nanocellulose fibers onto the micropatterned molds. The mold is pre-fabricated via deep reactive ion etching.³⁶ This method does not need manual operations and is straightforward, but the mold preparation is complicated and expensive. More importantly, all the above methods can only pattern millimeter-scale microchannels, and large channel dimension has compromised the advantages of microfluidic devices, such as low reagent volume consumption and high integration. To date, a facile nanopaper microchannel patterning technique that can produce micrometer-scale channels is yet to develop.

In this paper, we report a new microchannel patterning process on nanopaper, based on the convenient micro-

embossing technique. Compared with the existing methods, our method is free of sophisticated equipment, low-cost, ease-of-operation, and is highly accurate. The polytetrafluoroethylene (Teflon) film was selected to make the convex microchannel mold (by laser cutting), as Teflon has excellent chemical inertness and a nonsticky property. The mold was then used to emboss microchannels on the nanopaper gel membrane. An additional layer of nanopaper gel was bonded to the channel layer to form closed hollow channels. Using this patterning technique, we first demonstrated two basic microfluidic devices on nanopaper: laminar-mixer and droplet generator. We then developed an optical colorimetric sensor and surface-enhanced Raman microscopy (SERS) NanoPADs. The SERS substrate, made of silver nanoparticles, was *in situ* formed by supplying two chemical reagents (AgNO_3 and NaBH_4) into and reacted within the channel. The common Raman reporter, Rhodamine B (RhB), was the example sensing target. Thanks to the excellent optical transparency of nanopaper, an outstanding performance with a low limit of detection (LOD) was achieved (2 mM for glucose and 19 fM for RhB).

RESULTS AND DISCUSSION

Microembossing Process for Microchannel Patterning on Nanopaper. As shown in Figure 1, the microembossing process mainly includes six steps: (i) a polytetrafluoroethylene (Teflon) film was selected to make the convex microchannel mold by laser cutting, as Teflon has excellent chemical inertness and a nonsticky property, and then the mold was used to emboss microchannels on the filtered nanopaper. The thickness of the selected Teflon mold mainly influences the depth of the microchannel (the correlations of both will be given in the later section). (ii) The (2,2,6,6-tetramethylpiperidin-1-yl)oxyl (TEMPO)-oxidized NFC gel (0.1 wt % in distilled water) suspension was first heavily stirred until no cellulose floc can be observed. The clear suspension was then vacuum-filtered, and the nanopaper gel (4 cm in diameter) can be obtained. (iii and iv) This nanopaper gel was then embossed using the Teflon mold for a certain period of time under optimized embossing pressure and temperature. (v and vi) To form the hollow microchannel for functional NanoPADs, an additional layer of filter nanopaper gel was

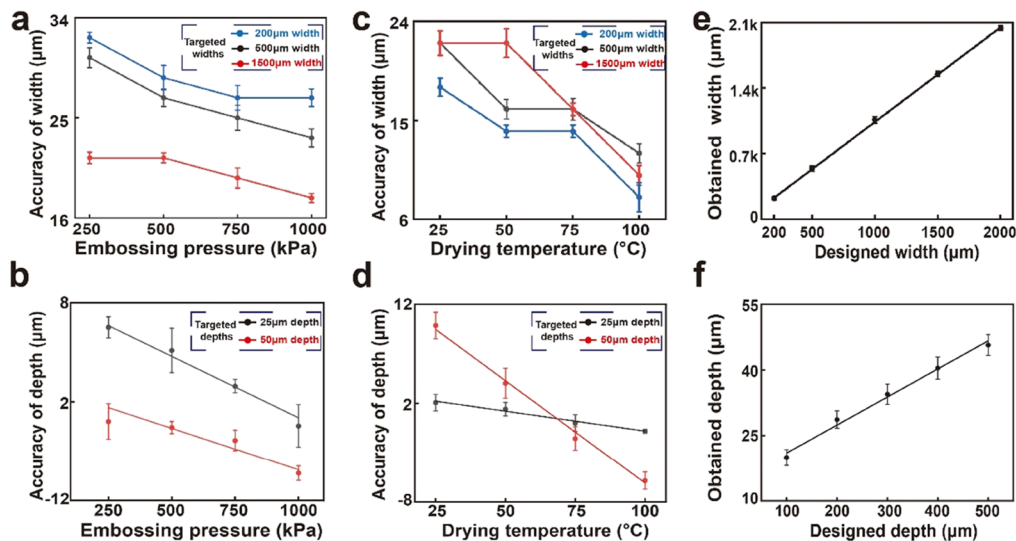


Figure 2. Optimization of microchannel embossing. The influences of embossing pressure (a, b) and drying temperature (c, d) on widths and depths' fabrication accuracy, respectively. Nanopaper microfluidic devices' design guidelines for channel widths (e) and depths (f) ($n = 5$). (The targeted: the widths and depths of microchannel expected; the obtained: the widths and depths of microchannels fabricated; the designed: the widths and depths of Teflon molds.)

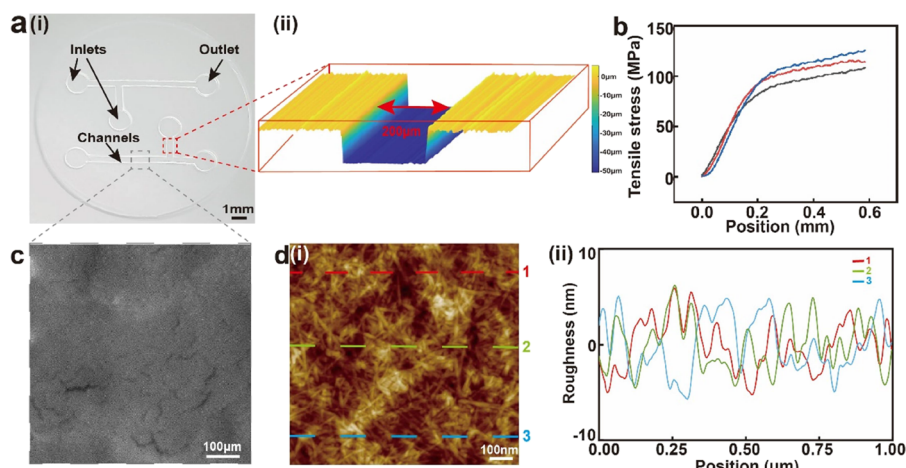


Figure 3. Characterization of embossed microchannels on NanoPADs. (a) Fabricated NanoPAD with a laser microscope generated a 3D channel view, showing the smooth surface of the fabricated microchannel. Scale bar: 1 mm. (b) Mechanical testing of microchannels ($n = 3$). (c) Scanning electron microscopy (SEM) image of the embossed microchannel. Scale bar: 500 μm. (d) Atomic force microscopy (AFM) image showing the roughness of the embossed microchannel in a $1 \mu\text{m} \times 1 \mu\text{m}$ area and surface roughness depth data along the three scanning lines. Scale bar: 100 nm.

peeled off from the filter membrane and was carefully attached on the embossed nanopaper gel layer. Those two layers of nanopaper gels bonded spontaneously in the drying oven by nanofiber diffusion (30 mins). Since the hydrogen bond of “gel-like” nanopaper is much stronger than that of fiber suspension and dried nanopaper, which makes nanocellulose fiber to entanglement and adhesion, two layers “gel-like” nanopaper can be bonded compactly by self-diffusion without any external force.^{7,37} The NanoPADs have good sealing performance and effectively avoid lateral fluid leakage. The entire fabrication process is less than 45 min (including 30 min drying time).

There are many parameters that influence the dimension accuracy of the embossed microchannels, such as the intrinsic properties (i.e., water weight ratio and thickness of the gel-like nanopaper membrane), and thereby these parameters are controlled to the constant values in our studies. The embossing

pressure and drying temperature are the two main processing parameters,⁷ which are investigated and optimized to improve the dimensional accuracy of the obtained microchannel. The accuracy is defined as the dimensional differences between the targeted and the obtained microchannels.

The embossing pressure was first studied, and it has been found that higher embossing pressure (250–1000 kPa) gives a better fabrication accuracy for a series of design widths and depths ($n = 5$). As shown in Figure 2a,b, higher embossing pressure contributes to tighter fiber structure arrangement of nanopaper gel;⁷ however, the pressure cannot become larger (>1000 kPa), since higher pressure will break the cellulose structure. Additionally, the larger targeted widths and depths also lead to better accuracy under the same embossing pressure, which could be explained by the more even pressure distribution in larger areas. For the embossing temperature, the results (Figure 2c,d) also indicated that higher temperature

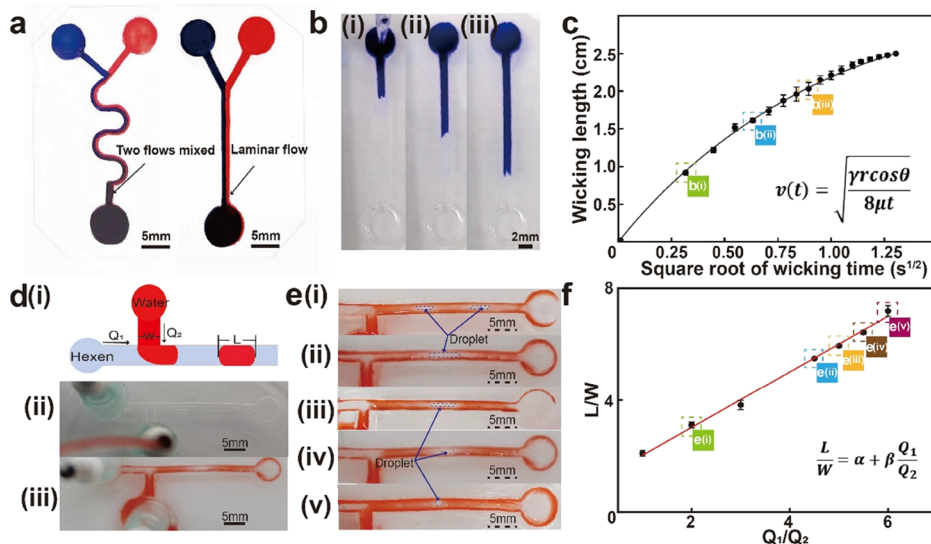


Figure 4. Fundamentals of fluidic behavior in the nanopaper microchannel. (a) Photographs of the nanopaper microfluidic mixer and laminar flow device. (b) Flow-wicking at different distances along the hollow channel. (c) Capillary performance along the hollow channel ($n = 5$). (d) Schematic illustration of the droplets inside the T-junction channel and the embossed device with the inlet tubes. (e) Droplet generator working at different frequencies. (f) Linear dependence on the flow rates of Q_1/Q_2 and L/W ($n = 5$).

(25–100 °C) has better channel accuracy for both widths and depths, since rapid dehydration and decarburation caused by high temperature lead to a tighter fiber structure and larger shrinkage of nanopaper gel.^{7,38} However, gel wrinkles once the temperature exceeds 75 °C and has low light transmittance, which compromises its excellence for optical sensing. Therefore, the optimized embossing parameters have been determined to be 750 kPa and 75 °C.

Based on the optimized embossing pressure and temperature, we also provided one quick look-up table (designed vs obtained dimension parameters) as the guideline for application developments (Figure 2e,f). The tables consist of common dimensional widths (200–2000 μm) and depths (10–50 μm) of the microfluidic devices, and it can be seen that the designed and obtained dimensions follow one liner first-order function relationship ($y = 0.06x + 15$; $n = 5$; x is the designed thickness of Teflon mold and y is the obtained depth of microchannel). This suggests that function can be used to design hollow channels with required depths for further applications. Moreover, the optimized processing conditions show good fabrication repeatability with low standard derations, while the highest variation for width and depth is 2.5 and 9%, respectively. For testing the mold durability, we compared the mechanical properties of Teflon mold before and after 1000 times embossing. There was no obvious degradation in terms of the scale of the mold in width, length, and depth (Table S1). The Young's modulus (0.55 GPa) of Teflon mold after the embossing process is nearly equal to that of the prepared mold (0.56 GPa), showing the high durability of Teflon mold.^{7,38}

Characterization of the NanoPADs after Embossing.

As shown in Figure 3a, one functional NanoPAD with T-junction microchannels was fabricated for characterization. From the quick look-up table, it has been found that 200 μm mold width corresponds to the 200 μm width of the obtained microchannel, which has also been confirmed by the laser microscope scanning (width = 202 μm) shown in Figure 3aii. The laser scanning image shows the rectangular microchannel with sharp corners (6.7% variation), where no excess

nanocellulose accumulated. To the best of our knowledge, the 200 μm width has been the smallest nanopaper microchannel reported by far. The small microchannel dimensions can bring many advantages, such as high device integration and low reagent consumptions, among others.

To understand whether the embossing process has damaged the surface structure of the nanopaper, SEM was used to compare the embossed area (microchannel) and the non-embossed area of the nanopaper, and no obvious differences in surface structures have been found (Figures 3c and S7). Additionally, we also characterized the surface homogeneity and roughness of nanopaper by AFM. We randomly selected two 1 μm × 1 μm areas from the microchannel and the nonembossed areas, respectively, and the microchannel's root mean square roughness was detected as 2.89 nm and was comparable to that of the intrinsic nanopaper (3.97 nm). The surface roughness depth data of the microchannel along the three scanning lines of the AFM image are shown in Figure 3diii. This low surface roughness is comparable to the results of other similar studies.⁹ Macroscopically, Figure 3a also demonstrates the ultrasMOOTH and transparent structure of our NanoPADs.

We also proved the optical stability of the embossing microchannel, using Fourier-transform infrared spectroscopy (FT-IR). It has been found that the light transmittance of nanopaper prepared is more than 88% in the wavelength range of 400–800 nm. As the NanoPADs could be stored and transported for potential real-world use, the optical stability is also critical and the optical transparency decreased 0.90% after one-month shelf time (Figure S3), which could be explained by the slight aging of carbon-containing organics.³⁹ We also measured the mechanical properties of the nanopaper and found no obvious degradation in terms of Young's modulus and tensile strength after the embossing process ($n = 3$). Figure 3b illustrates the relationship between the tensile length and stress, while with the increase of the tensile distance, the stress on embossed channels also increased until the breaking point. After embossing, the nanopaper still possesses good mechanical properties (Young's modulus = 6.30 GPa (after) and 6.35

GPa (before)) and can be used as an excellent substrate material for functional devices such as NanoPADs.

Fundamentals of Fluidic Behavior in NanoPADs. To demonstrate the capability of the NanoPADs, we first built two fundamental types of microfluidic devices: the continuous flow device and the droplet generators on nanopaper. Within the continuous flow microfluidic device, the laminar flow is the fundamental phenomenon that fluid flows in layers.^{40,41} Many attractive applications have been developed based on this phenomenon, such as the creation of DNA analysis equipment⁴² and multibiological detection.⁴³ Because of the low Reynolds number of layers in microfluidic devices, mixer flow is difficult to be realized. We demonstrated a curved microchannel, which is the most basic fluidic channel design for a microfluidic mixer. Figure 4a shows laminar flow (1 mm width, 25 mm length, and 50 μm depth) behavior in the nanopaper microchannel. Furthermore, the microfluidic mixer is also one of the fundamental applications and can be achieved by using the S-curve microchannels, shown in Figure 4a. It shows that the red and blue solutions successfully mixed at the end of the curved channel, due to radial flow provided by shear stress.⁴⁴

We also characterized the flow-wicking performance inside the microchannel on nanopaper and found that fluids flow at a much faster rate than that in the regular cellulose paper-based channel (Movie S1).⁴⁵ To avoid the influences of the fluidic flow's initial speed, the same volume of the water droplets was vertically added to the inlets of the microchannel. Figure 4b,c shows flow-wicking at different distances and speeds along the hollow channel, respectively ($n = 5$). We found that the wicking flow speed decreased with the increase of the travel distance from the inlet zone through the capillary force of the hydrophilic inner wall and gradually stabilized, which is theoretically supported by the Lucas–Washburn equation⁴⁶ (1):

$$v(t) = \sqrt{\frac{\gamma r \cos\theta}{8\mu t}} \quad (1)$$

where $v(t)$ is the speed of the advancing liquid front under capillary pressure into a channel, t is the time to access the channel, γ is the surface tension, θ is the contact angle, μ is the dynamic viscosity of the liquid, and r is the effective capillary radius of the rectangular channel. The characterization results can be used to design hollow channels with the required flow velocity.

Another major type of microfluidic application is the droplet generator, where the droplets are generated by accurately controlling two immiscible liquids (usually water and oil) into a T-junction channel, and the shear force decomposes the liquid into droplets.^{47–49} To realize droplet generators, dyed water and hexadecane (oil) were streamed into a two-inlet "T" channel (Figure 4di). Figure 4ei shows the droplet generator obtained using identical flow rates of the water and hexadecane flow, and by altering the flow rates, different sizes of the droplets can also be obtained under different frequency (Figure 4e). This behavior is governed by the one simple scaling eq 2^{50–52} and is also constant with our experimental observations (Figure 4f):

$$\frac{L}{W} = \alpha + \beta \frac{Q_1}{Q_2} \quad (2)$$

Consider a nominal case for a T-junction generator where $\alpha = 1$, $\beta = 1$, L is the length, W is the width of the droplet, and Q_1 and Q_2 are the flow rates of water and hexadecane respectively. Because each droplet can be controlled, separated, or analyzed, droplet generators have high potential in biomedical applications, such as encapsulation therapy.^{53,54}

Colorimetric Detection of Glucose in NanoPADs.

Diabetes is one of the most common diseases in the world, and its associated complications lead to disability and shortened life span.^{55,56} Though various colorimetric glucose sensors have been demonstrated on μ PADs, the opacity of regular paper degraded the colorimetric detection, and thereby the sensitivity of such sensors is usually limited.^{57,58} In this research, high optical transparency of the nanopaper can effectively facilitate the transmittance of the colorimetric detection and enables high sensitivity. The principle of glucose colorimetric detection is shown in Figure 5a, and the double

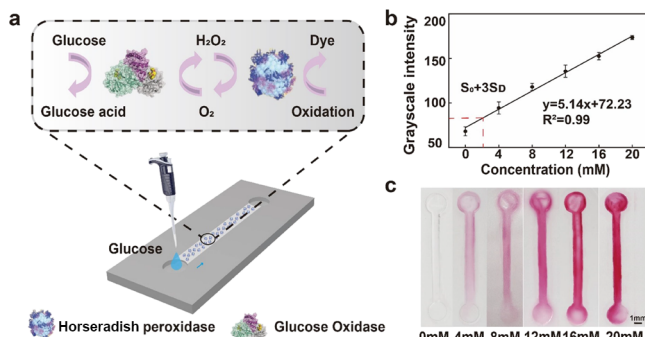


Figure 5. Glucose colorimetric detection. (a) Schematic of the principle for glucose colorimetric detection. (b) Calibration curve of the colorimetric grayscale intensity as a function of the glucose concentration ($n = 5$). (c) Photograph shows colorimetric signals in hollow channels after reacting for 10 min at different concentrations of glucose.

enzyme (glucose oxidase and peroxidase type I) system is used to amplify the color signal while one enzyme is catalytically linked to another.⁵⁹ To perform a test, 5 μL of the enzymic solution was first wicked into a hollow channel (500 μm width, 25 mm length, and 50 μm depth) and dried at room temperature for 10 min. Then, 5 μL of artificial urine dissolved with different glucose concentrations was added into the channel for reaction. Figure 5c shows the photographs of urine samples with varying concentrations of glucose (0 to 20 mM), while the photographs of the microchannels were measured after reacting for 10 min using a desktop scanner (CanoScan LiDE 300, Cannon, Japan). ImageJ was used to quantify the average grayscale intensity of the hollow channels. By using the grayscale intensity as the readout, we obtained the linear calibration curve of the glucose sensor (Figure 5b). The LOD for glucose detection is calculated as 2 mM, which is defined as the glucose concentration corresponding to the blank control intensity plus three times the standard deviation of the blank control color intensity.⁶⁰ The calibration curve also satisfied the first-order relationship with the concentration of glucose between 0 and 20 mM ($y = 5.14x + 72.23$) and the R^2 square was 0.99, which demonstrates its feasibility in the colorimetric sensing applications. Due to the excellent optical transparency with low reflectivity of NanoPADs, the LOD outperforms most regular paper-based detection without chemical functionalization (2.5 mM),⁶¹ and is similar to the sensitivity results on

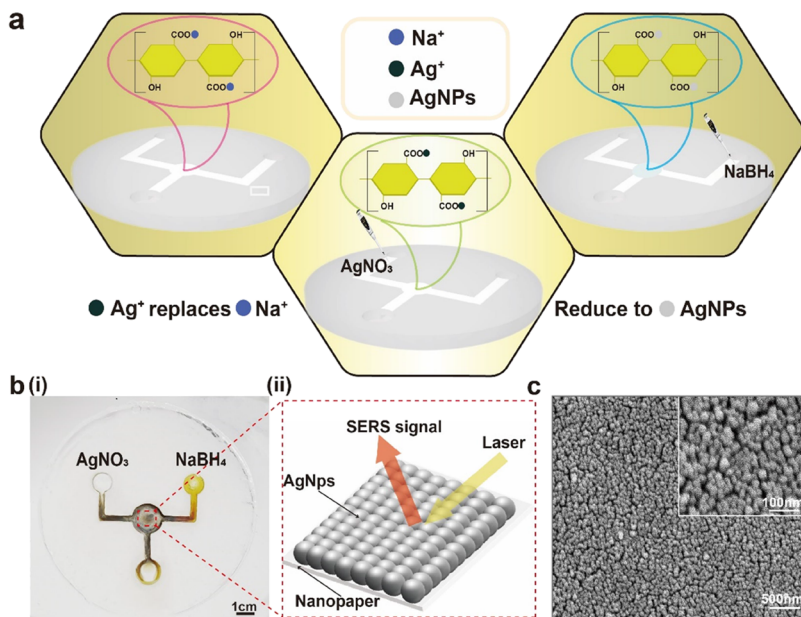


Figure 6. Sensitive SERS sensing of small molecules on NanoPADs. (a) Schematic of AgNPs growth on the detection zone of the NanoPADs. (b) Photograph of NanoPADs after AgNPs growth and schematic of the SERS-based molecule detection. (c) SEM image of the *in situ* grown AgNPs on NanoPADs shows a dense and organized AgNPs array.

PDMS devices maintaining the advantages of being cost-effective and environmentally friendly. For instance, NanoPADs can be widely applied in other colorimetric detection with high sensitivity, such as trace element analysts and uric acid in the future.

Sensitive SERS-Based Chemical Sensing of Small Molecules on NanoPADs. SERS is a label-free and highly sensitive method for detecting and analyzing biological and chemical analytes.^{62–65} Silver nanoparticles (AgNPs) have been commonly used as the SERS substrate because of their high molar extinction coefficient and excellent optical properties.^{66,67} Usually, the highly organized and dense AgNPs arrays can enable the highly sensitive SERS sensing, and thereby one *in situ* method for growing AgNPs in the detection zone of the NanoPADs was used. The design of the SERS-NanoPADs is shown in Figure 6a, and it consists of two microchannels that meet in the detection zone (circular area labeled in Figure 6b). The *in situ* method was based on the simple ion layer absorption and reaction process.^{68,69} Briefly, AgNPs were formed by replacing the positive ions on the carboxyl group of the reaction zone with silver ions and then using BH⁴⁻ to reduce Ag⁺ on the paper surface shown in Figure 6a. The Ag⁺ was efficiently absorbed on the surface of nanopaper by carboxyl groups through electrostatic interaction, and BH⁴⁻ has strong reducibility to silver ions.^{70,71} Figure 6b shows the photograph of the NanoPADs with *in situ* grown AgNPs which are ready for testing. We also characterized the AgNPs by SEM imaging and found that the dense, uniform, and well-organized AgNPs arrays were formed with the average 55 nm diameter of AgNPs (Figure 6c), and the diameter distribution histogram is shown in Figure S10.

To demonstrate the developed SERS-NanoPADs in real-world applications, the common environmental pollutant and low-toxicity organic chemical substance, RhB and melamine (C₃H₆N₆), were selected as the sensing examples. The RhB molecules were directly mixed with ethanol, while the melamine was mixed with the milk powder, as the melamine

is the common fake agent in infant milk powders. Five microliters of the above solution was added into the hollow channel from the sensing solution inlet, and then the Raman signal in the reaction zone was quantified. Figure 7a shows the

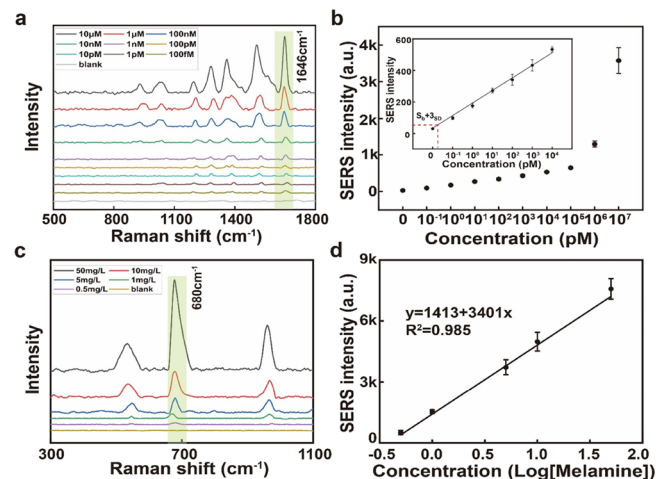


Figure 7. SERS-based detection of RhB and melamine. (a) Raman spectra of RhB at concentrations of 100 fM to 10 μ M. (b) Calibration of RhB at 1646 cm^{-1} ($n = 5$). (c) Raman spectra of melamine at concentrations of 0.5 to 50 $\mu\text{g}/\text{mL}$. (d) Calibration of melamine at 680 cm^{-1} ($n = 5$).

Raman spectra of RhB samples at different concentrations (100 fM–10 μ M) in ethanol, and pure ethanol was chosen as the blank control. The spectra measured contain strong RhB bands, including the xanthene ring puckering mode (1200 cm^{-1}), C–O–C stretching (1280 cm^{-1}), C–C stretching (1350 cm^{-1}), C–N stretching (1384 cm^{-1}), C–H stretching (1520 cm^{-1}), and aromatic C–C stretching (1646 cm^{-1}).^{72,73} We used 1646 cm^{-1} peak intensity as the reading because this band intensity is more sensitive to RhB concentration with low background noise.^{9,74} The calibration curve of RhB detection is

shown in Figure 7b, and the LOD was calculated to be 19 fM, defined as the RhB concentration corresponding to the blank control intensity plus three times the standard deviation of the Raman intensity of the blank control. Figure 7c shows the Raman spectra of melamine samples in infant formula at different concentrations (0.5 to 50 $\mu\text{g/mL}$). These spectra revealed all the prominent characteristic Raman bands of melamine at 545 cm^{-1} (N–N stretching), 680 cm^{-1} (the ring-breathing II mode of the triazine ring), and 956 cm^{-1} (the ring-breathing mode I of the triazine ring).⁷⁵ Since the 680 cm^{-1} peak was more representative of all the concentrations, the equation of the concentration-dependent SERS intensity at this peak is expressed by $y = 3401 \times \log C_m + 1413$, where C_m represents the doped concentration of melamine in infant formula. The LOD value of melamine in infant formula was estimated to be 0.38 $\mu\text{g/mL}$ (Figure 7d).

RhB, a small molecule, is commonly used to calculate the Raman enhancement factor (EF) to evaluate the SERS activity of our NanoPADs. The EF was calculated as $\text{EF} = \frac{I_{\text{SERS}}}{I_{\text{bare}}} \times \frac{C_{\text{bare}}}{C_{\text{SERS}}}$,

where I_{SERS} and C_{SERS} are the intensities of the Raman spectra at 1646 cm^{-1} with the SERS effect and concentrations on AgNPs-coated NanoPADs, and I_{bare} and C_{bare} are on bare NanoPADs. Therefore, the EF was calculated to be 1.34×10^9 , which is superior for high-sensitivity optical sensing applications compared with traditional transparent substrates such as glass or PDMS ($>10^6$) microfluidic devices.⁷⁶ There are several reasons that could explain this outstanding performance. First, the highly integrated and facile fabrication process of NanoPADs can effectively avoid pollution in the fabrication process and the interference of introducing other impurities. Second, we demonstrated a microfluidic device assisted *in situ* AgNPs growth process by supplying two chemical reagents (AgNO_3 and NaBH_4) into and reacted within the detection zone compared with successive ionic layer adsorption and reaction process.⁸ Third, NanoPADs represent better performance than regular paper (the EF and LOD based on *in situ* AgNPs can only achieve as 1.1×10^9 and 10 pM⁷⁷), since the high optical transparency of NanoPADs reduces signal loss by light reflection and special nanocellulose carboxyl structure provides uniform growth of *in situ* AgNPs.

CONCLUSIONS

In summary, a new microchannel patterning process on nanopaper based on the convenient microembossing technique with the facile plastic micro-molds was developed. Importantly, for the first time, patterning microchannels on nanopaper is down to 200 μm , which is 4 times better than the existing methods. After the optimization of patterning parameters, the guidelines show good fabrication repeatability with low standard deviations (the highest variation for width and depth is 2.5 and 9%, respectively), and we also provide one quick look-up table as the guideline for application developments. Consequently, two functional analytical sensors for colorimetric glucose detection and SERS biosensing have also been demonstrated on the NanoPADs with low LOD (2 mM for glucose and 19 fM for RhB). In the future, with the application of micro-nano printing and high-precision cutting technology, the scale of molds and corresponding microchannels will down to dozens of microns. Though those methods are contrary to time-saving and cost-effective, they may spark the further application of nanopaper. We believe that these new fundamental microchannel fabrication methods will spark

new designs and applications in the emerging field of nanopaper-based microfluidic chemical and biomedical sensing applications.

METHODS

Reagents and Materials. TEMPO-oxidized NFC slurry (1.0 wt % solid, carboxylate level 2.0 mmol/g solid, average nanofiber diameter: 10 nm) was purchased from Tianjin University of Science and Technology. Melamine (>99%), Rhodamine B (RhB, >95%), hexadecane (>99%), and trehalose (>99%) were obtained from Macklin (Shanghai, China). AgNO_3 (99%) and ethanol (>99%) were ordered from Hushi (Shanghai). NaBH_4 (>98%), 3,5-dichloro-2-hydroxy-benzenesulfonic acid (>99%), and peroxidase type I (from horseradish, 200 U mg^{-1}) were purchased from Aladdin (Shanghai, China). 4-aminoantipyrine (>98%) and D-(+)-Glucose (>99%) were obtained from Meryer (Shanghai, China). Teflon films were made from Shenzhen Huashenglong plastic material Co., Ltd. (Shenzhen, China). Polyethylene terephthalate (PET) was ordered from Myers Industries (Akron, USA). Infant formula was purchased from the local supermarket.

Optimization of Embossed Microchannels on Nanopaper. The 4.0 g TEMPO-oxidized NFC slurry was dispersed in distilled water to a final content of 0.1 wt %, and the suspension was stirred at 800 rpm for 30 min. 400 g of the prepared suspension was vacuum-filtered for 4 h with a PVDF filter membrane (VVLPO4700, EMD Millipore Corporation, pore size: 0.1 μm) on a glass filter holder. The prepared cut Teflon molds (designed by AutoCAD 2019 (Autodesk, San Rafael, CA) and cut by laser cutting machine (Han's Yuming Laser CMA0604-B-A, China)) by requirement. Next, the filtered nanopaper gel with the cut Teflon molds on it was placed between two PET films and hot-pressed under different pressure at a high temperature for 10 min to form. After releasing the molds, an additional layer of nanopaper gel was bonded and stored in the oven for drying under different temperature for around 1 h.

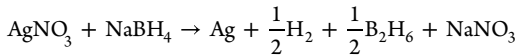
Characterization. In order to understand whether embossing has a significant effect on the structure of the paper, the cross-sectional image of the embossed microchannel was characterized by a laser microscope (KEYENCE VK-X150, Japan). An ultrafast atomic force microscope (Bruker Dimension Icon, Germany) was used to characterize the surface of NanoPADs. A tensile test was conducted to determine the mechanical strength of the nanopaper with a universal testing machine (INSTRON 3343, USA, the loading cell is 1 kN). A strip (5 mm \times 25 mm) was prepared for the tensile test. SEM (FEI Scios 2 HiVac, USA) was used to characterize the embossed channel and morphology of AgNPs at a working voltage of 5 kV. The transmittance of the nanopaper was obtained by an FT-IR (Thermo Scientific Nicolet iS20, USA).

Glucose Colorimetric Detection. The biomarker analyte in the colorimetric test was D-(+)-glucose. Glucose colorimetric detection depends on the use of glucose oxidase. Glucose oxidation is catalyzed by oxygen to produce gluconic acid and hydrogen peroxide. The oxidation of chromogenic agents measures the product of H_2O_2 in the presence of peroxidase. Therefore, 120 U mL^{-1} glucose oxidase (from *Aspergillus niger*, 180 U mg^{-1}) mixed with 30 U mL^{-1} peroxidase type I (from horseradish, 200 U mg^{-1}) was used as a stabilizer. The oxidation indicator was prepared by a mixture of 0.2 M 4-aminoantipyrine and 0.4 M sodium 3,5-dichloro-2-hydroxy-benzenesulfonate. The artificial urine solution contains 2.5 mM calcium chloride, 2 mM citric acid, 90 mM sodium chloride, 1.1 mM lactic acid, 2 mM magnesium sulfate, 10 mM sodium sulfate, 7 mM potassium dihydrogen phosphate, 170 mM urea, 25 mM sodium bicarbonate, 7 mM potassium dihydrogen phosphate, and 25 mM ammonium chloride (pH = 6).^{78–80}

Above glucose detection reagents were dissolved in 1× phosphate buffer saline (PBS) solution. Different concentrations of glucose were diluted in the artificial urine solution for detection. Five microliters of glucose detection reagent solution was wicked into a hollow channel and dried at room temperature for 10 min. Then 5 μL of artificial

urine dissolved with different glucose concentrations was added into the channel for reaction.

AgNP Growth. AgNPs were grown in the detection zone of the flow channel by the improved successive ionic layer adsorption and reaction process. The chemical reactions involved in the process are represented by the following formula:⁷⁷



AgNO_3 and NaBH_4 were used as silver precursors and reducing agents, respectively.

In brief, 5 μL of the 20 mM AgNO_3 was dropped in the left inlet zone of the channel and preserved in the reaction zone for 30 s. The above process was repeated five times, as in this condition, the distribution of AgNPs is uniform without agglomeration and can be accounted for the higher band intensity.⁸ Five microliters of distilled water was dropped in the right inlet zone for washing. Then 5 μL of 20 mM NaBH_4 was added to the right inlet zone.

SERS Measurement. All Raman spectra were measured by Horiba Xplo RA (Japan) with a 532 nm laser and a 50 \times objective. RhB has dissolved in ethanol with tenfold dilution from 10×10^{-6} to 100×10^{-15} M. The Raman spectrum was acquired in the region of 500 to 1800 cm^{-1} with a spectral resolution of 2 cm^{-1} . For melamine, first, melamine and infant formula were dissolved in distilled water to prepare 1 and 5 g/L solution, respectively. Melamine solution was dissolved in infant formula solution with concentrations varying from 0.5 to 50 mg/L. The Raman spectrum was acquired in the 300 to 1100 cm^{-1} with a spectral resolution of 2 cm^{-1} . Five microliters of the analyte solution was dropped on the inlet zone of the channel and dried to detect the SERS activity in the reaction zone. Raman spectra are taken from the average of five measurements. All spectral data were analyzed using Origin lab software. A baseline correction procedure was performed to obtain the final spectrum for each measurement.

ASSOCIATED CONTENT

Supporting Information

The Supporting Information is available free of charge at <https://pubs.acs.org/doi/10.1021/acsami.2c19354>.

NanoPAD fabrication process, transmittance data of the NanoPAD produced after 1 week and 1 month, summary of the coefficient of variation and Reynolds numbers of droplet generators under different flow frequency and coefficients of variation of glucose colorimetric detection at different concentrations, RhB SERS detection at different concentrations, and melamine SERS detection at different concentrations ([PDF](#))

Video depicting fluid flowing at a much faster rate in the embossed hollow microchannel on nanopaper than that in the regular cellulose paper-based channel ([MP4](#))

AUTHOR INFORMATION

Corresponding Authors

Eng Gee Lim – School of Advanced Technology, Xi'an Jiaotong - Liverpool University, Suzhou 215123, China; Department of Electrical Engineering and Electronics, University of Liverpool, Liverpool L69 7ZX, U.K.; Phone: +86 (0)51288161405; Email: enggee.lim@xjtu.edu.cn

Xinyu Liu – Department of Mechanical and Industrial Engineering, University of Toronto, Toronto, Ontario M5S 2E8, Canada; orcid.org/0000-0001-5705-9765; Phone: +1-416-946-0558; Email: Xyliu@mie.utoronto.ca

Pengfei Song – School of Advanced Technology, Xi'an Jiaotong - Liverpool University, Suzhou 215123, China; Department of Electrical Engineering and Electronics, University of Liverpool, Liverpool L69 7ZX, U.K.; Phone: +86 (0)512 81889039; Email: Pengfei.Song@xjtu.edu.cn

Authors

Wenwen Yuan – School of Advanced Technology, Xi'an Jiaotong - Liverpool University, Suzhou 215123, China; Department of Electrical Engineering and Electronics, University of Liverpool, Liverpool L69 7ZX, U.K.

Hang Yuan – School of Advanced Technology, Xi'an Jiaotong - Liverpool University, Suzhou 215123, China; orcid.org/0000-0002-8079-7413

Keran Jiao – School of Advanced Technology, Xi'an Jiaotong - Liverpool University, Suzhou 215123, China

Jia Zhu – School of Advanced Technology, Xi'an Jiaotong - Liverpool University, Suzhou 215123, China; School of Intelligent Manufacturing and Transportation, Suzhou City University, Suzhou 215000, China; Department of Electrical Engineering and Electronics, University of Liverpool, Liverpool L69 7ZX, U.K.

Ivana Mitrovic – Department of Electrical Engineering and Electronics, University of Liverpool, Liverpool L69 7ZX, U.K.

Sixuan Duan – School of Advanced Technology, Xi'an Jiaotong - Liverpool University, Suzhou 215123, China; Department of Electrical Engineering and Electronics, University of Liverpool, Liverpool L69 7ZX, U.K.

Yongjie Wang – School of Science, Harbin Institute of Technology - Shenzhen, Shenzhen 518055, China

Shan Cong – School of Nano-Tech and Nano-Bionics, University of Science and Technology of China, Hefei 230026, China; orcid.org/0000-0002-5305-1237

Chun Zhao – School of Advanced Technology, Xi'an Jiaotong - Liverpool University, Suzhou 215123, China; Department of Electrical Engineering and Electronics, University of Liverpool, Liverpool L69 7ZX, U.K.; orcid.org/0000-0002-4783-960X

Jie Sun – School of Advanced Technology, Xi'an Jiaotong - Liverpool University, Suzhou 215123, China; Department of Electrical Engineering and Electronics, University of Liverpool, Liverpool L69 7ZX, U.K.

Complete contact information is available at:

<https://pubs.acs.org/10.1021/acsami.2c19354>

Author Contributions

All authors have given approval to the final version of the manuscript.

Notes

The authors declare no competing financial interest.

ACKNOWLEDGMENTS

The authors acknowledge the financial support from the programs of Natural Science Foundation of the Jiangsu Higher Education (20KJB460024, 22KJB460033), Jiangsu Science and Technology Programme - Young Scholar (BK2020041995), Jiangsu Province High-level Innovation and Entrepreneurship Talent Plan (2020-30803), XJTLU Key Programme Special Fund – Exploratory Research Programme (KSF-E-39), and XJTLU Research Development Fund (RDF-18-02-20). The authors also acknowledge the financial support from Xi'an

Jiaotong – Liverpool University to W. Yuan (PGRS1906040) and S. Duan (PGRS1912019).

■ REFERENCES

- (1) Zhu, H.; Fang, Z.; Preston, C.; Li, Y.; Hu, L. Transparent Paper: Fabrications, Properties, and Device Applications. *Energy Environ. Sci.* **2014**, *7*, 269–287.
- (2) Nogi, M.; Iwamoto, S.; Nakagaito, A. N.; Yano, H. Optically Transparent Nanofiber Paper. *Adv. Mater.* **2009**, *21*, 1595–1598.
- (3) Lavoine, N.; Desloges, I.; Dufresne, A.; Bras, J. Microfibrillated Cellulose – Its Barrier Properties and Applications in Cellulosic Materials: A Review. *Carbohydr. Polym.* **2012**, *90*, 735–764.
- (4) Barhoum, A.; Samyn, P.; Öhlund, T.; Dufresne, A. Review of Recent Research on Flexible Multifunctional Nanopapers. *Nanoscale* **2017**, *9*, 15181–15205.
- (5) Dufresne, A. Nanocellulose: A New Ageless Bionanomaterial. *Mater. Today* **2013**, *16*, 220–227.
- (6) Martin-Martinez, F. J. Designing Nanocellulose Materials from the Molecular Scale. *Proc. Natl. Acad. Sci. U. S. A.* **2018**, *115*, 7174–7175.
- (7) Sehaqui, H.; Liu, A.; Zhou, Q.; Berglund, L. A. Fast Preparation Procedure for Large, Flat Cellulose and Cellulose/Inorganic Nanopaper Structures. *Biomacromolecules* **2010**, *11*, 2195–2198.
- (8) Chen, L.; Ying, B.; Song, P.; Liu, X. A Nanocellulose-Paper-Based SERS Multiwell Plate with High Sensitivity and High Signal Homogeneity. *Adv. Mater. Interfaces* **2019**, *6*, No. 1901346.
- (9) Ying, B.; Park, S.; Chen, L.; Dong, X.; Young, K.; Liu, X. NanoPADs and NanoFACEs: An Optically Transparent Nanopaper-Based Device for Biomedical Applications. *Lab Chip* **2020**, *20*, 3322–3333.
- (10) Sehaqui, H.; Zhou, Q.; Ikkala, O.; Berglund, L. A. Strong and Tough Cellulose Nanopaper with High Specific Surface Area and Porosity. *Biomacromolecules* **2011**, *12*, 3638–3644.
- (11) Fang, Z.; Zhu, H.; Yuan, Y.; Ha, D.; Zhu, S.; Preston, C.; Chen, Q.; Li, Y.; Han, X.; Lee, S.; Chen, G.; Li, T.; Munday, J.; Huang, J.; Hu, L. Novel Nanostructured Paper with Ultrahigh Transparency and Ultrahigh Haze for Solar Cells. *Nano Lett.* **2014**, *14*, 765–773.
- (12) Hu, L.; Zheng, G.; Yao, J.; Liu, N.; Weil, B.; Eskilsson, M.; Karabulut, E.; Ruan, Z.; Fan, S.; Bloking, T.; McGehee, D.; Wågberg, L.; Cui, Y. Transparent and Conductive Paper from Nanocellulose Fibers. *Energy Environ. Sci.* **2013**, *6*, 513–518.
- (13) Zheng, G.; Cui, Y.; Karabulut, E.; Wågberg, L.; Zhu, H.; Hu, L. Nanostructured Paper for Flexible Energy and Electronic Devices. *MRS Bull.* **2013**, *38*, 320–325.
- (14) Koga, H.; Saito, T.; Kitaoka, T.; Nogi, M.; Suganuma, K.; Isogai, A. Transparent, Conductive, and Printable Composites Consisting of TEMPO-Oxidized Nanocellulose and Carbon Nanotube. *Biomacromolecules* **2013**, *14*, 1160–1165.
- (15) Cheng, F.; Cao, X.; Li, H.; Liu, T.; Xie, X.; Huang, D.; Maharjan, S.; Bei, H. P.; Gómez, A.; Li, J.; Zhan, H.; Shen, H.; Liu, S.; He, J.; Zhang, Y. S. Generation of Cost-Effective Paper-Based Tissue Models through Matrix-Assisted Sacrificial 3D Printing. *Nano Lett.* **2019**, *19*, 3603–3611.
- (16) Huang, J.; Zhu, H.; Chen, Y.; Preston, C.; Rohrbach, K.; Cumings, J.; Hu, L. Highly Transparent and Flexible Nanopaper Transistors. *ACS Nano* **2013**, *7*, 2106–2113.
- (17) Martinez, A. W.; Phillips, S. T.; Butte, M. J.; Whitesides, G. M. Patterned Paper as a Platform for Inexpensive, Low-Volume Portable Bioassays. *Angew. Chem., Int. Ed.* **2007**, *46*, 1318–1320.
- (18) Rolland, J. P.; Mourey, D. A. Paper as a Novel Material Platform for Devices. *MRS Bull.* **2013**, *38*, 299–305.
- (19) Chin, C. D.; Linder, V.; Sia, S. K. Lab-on-a-Chip Devices for Global Health: Past Studies and Future Opportunities. *Lab Chip* **2007**, *7*, 41–57.
- (20) Chin, C. D.; Laksanasopin, T.; Cheung, Y. K.; Steinmiller, D.; Linder, V.; Parsa, H.; Wang, J.; Moore, H.; Rouse, R.; Umvilighozo, G.; Karita, E.; Mwambarangwe, L.; Braunstein, S. L.; van de Wijgert, J.; Sahabo, R.; Justman, J. E.; El-Sadr, W.; Sia, S. K. Microfluidics-Based Diagnostics of Infectious Diseases in the Developing World. *Nat. Med.* **2011**, *17*, 1015–1019.
- (21) Martinez, A. W.; Phillips, S. T.; Whitesides, G. M.; Carrilho, E. Diagnostics for the Developing World: Microfluidic Paper-Based Analytical Devices. *Anal. Chem.* **2010**, *82*, 3–10.
- (22) Carrilho, E.; Martinez, A. W.; Whitesides, G. M. Understanding Wax Printing: A Simple Micropatterning Process for Paper-Based Microfluidics. *Anal. Chem.* **2009**, *81*, 7091–7095.
- (23) Lu, Y.; Shi, W.; Qin, J.; Lin, B. Fabrication and Characterization of Paper-Based Microfluidics Prepared in Nitrocellulose Membrane By Wax Printing. *Anal. Chem.* **2010**, *82*, 329–335.
- (24) Cheng, C.-M.; Martinez, A. W.; Gong, J.; Mace, C. R.; Phillips, S. T.; Carrilho, E.; Mirica, K. A.; Whitesides, G. M. Paper-Based ELISA. *Angew. Chem.* **2010**, *122*, 4881–4884.
- (25) Murdock, R. C.; Shen, L.; Griffin, D. K.; Kelley-Loughnane, N.; Papautsky, I.; Hagen, J. A. Optimization of a Paper-Based ELISA for a Human Performance Biomarker. *Anal. Chem.* **2013**, *85*, 11634–11642.
- (26) Cai, T.; Duan, S.; Fu, H.; Zhu, J.; Lim, E. G.; Huang, K.; Hoettges, K.; Liu, X.; Song, P. A Paper-Based Microfluidic Analytical Device with A Highly Integrated On-Chip Valve For Autonomous ELISA. In *2022 IEEE 35th International Conference on Micro Electro Mechanical Systems Conference (MEMS)*, 2022; pp 271–274.
- (27) Nie, Z.; Nijhuis, A.; Gong, J.; Chen, X.; Kumachev, A.; Martinez, W.; Narovlyansky, M.; Whitesides, M. Electrochemical Sensing in Paper-Based Microfluidic Devices. *Lab Chip* **2010**, *10*, 477–483.
- (28) Li, X.; Zhao, C.; Liu, X. A Paper-Based Microfluidic Biosensor Integrating Zinc Oxide Nanowires for Electrochemical Glucose Detection. *Microsyst. Nanoeng.* **2015**, *1*, 15014.
- (29) Tenda, K.; van Gerven, B.; Arts, R.; Hiruta, Y.; Merkx, M.; Citterio, D. Paper-Based Antibody Detection Devices Using Bioluminescent RET-Switching Sensor Proteins. *Angew. Chem., Int. Ed.* **2018**, *57*, 15369–15373.
- (30) Holstein, C. A.; Chevalier, A.; Bennett, S.; Anderson, C. E.; Keniston, K.; Olsen, C.; Li, B.; Bales, B.; Moore, D. R.; Fu, E.; Baker, D.; Yager, P. Immobilizing Affinity Proteins to Nitrocellulose: A Toolbox for Paper-Based Assay Developers. *Anal. Bioanal. Chem.* **2016**, *408*, 1335–1346.
- (31) Gan, W.; Zhuang, B.; Zhang, P.; Han, J.; Li, C.-X.; Liu, P. A Filter Paper-Based Microdevice for Low-Cost, Rapid, and Automated DNA Extraction and Amplification from Diverse Sample Types. *Lab Chip* **2014**, *14*, 3719–3728.
- (32) Gong, M. M.; Nosrati, R.; San Gabriel, M. C.; Zini, A.; Sinton, D. Direct DNA Analysis with Paper-Based Ion Concentration Polarization. *J. Am. Chem. Soc.* **2015**, *137*, 13913–13919.
- (33) Liu, Y.; Li, R.; Liang, F.; Deng, C.; Seidi, F.; Xiao, H. Fluorescent Paper-Based Analytical Devices for Ultra-Sensitive Dual-Type RNA Detections and Accurate Gastric Cancer Screening. *Biosens. Bioelectron.* **2022**, *197*, No. 113781.
- (34) Kim, H.; Hyoung Lee, K.; Il Han, S.; Lee, D.; Chung, S.; Lee, D.; Hoon Lee, J. Origami-Paper-Based Device for Microvesicle/Exosome Preconcentration and Isolation. *Lab Chip* **2019**, *19*, 3917–3921.
- (35) Shin, S.; Hyun, J. Matrix-Assisted Three-Dimensional Printing of Cellulose Nanofibers for Paper Microfluidics. *ACS Appl. Mater. Interfaces* **2017**, *9*, 26438–26446.
- (36) Browne, C.; Garnier, G.; Batchelor, W. Moulding of Micropatterned Nanocellulose Films and Their Application in Fluid Handling. *J. Colloid Interface Sci.* **2021**, *587*, 162–172.
- (37) Päkkö, M.; Ankerfors, M.; Kosonen, H.; Nykänen, A.; Ahola, S.; Österberg, M.; Ruokolainen, J.; Laine, J.; Larsson, P. T.; Ikkala, O.; Lindström, T. Enzymatic Hydrolysis Combined with Mechanical Shearing and High-Pressure Homogenization for Nanoscale Cellulose Fibrils and Strong Gels. *Biomacromolecules* **2007**, *8*, 1934–1941.
- (38) Weishaupl, R.; Siqueira, G.; Schubert, M.; Tingaut, P.; Maniura-Weber, K.; Zimmermann, T.; Thöny-Meyer, L.; Faccio, G.; Ihssen, J. TEMPO-Oxidized Nanofibrillated Cellulose as a High

- Density Carrier for Bioactive Molecules. *Biomacromolecules* **2015**, *16*, 3640–3650.
- (39) Hamed, S. A. A. K.; Hassan, M. L. A New Mixture of Hydroxypropyl Cellulose and Nanocellulose for Wood Consolidation. *J. Cult. Herit.* **2019**, *35*, 140–144.
- (40) Abraham, S. B. Laminar Flow in Channels with Porous Walls. *J. Appl. Phys.* **1953**, *24*, 1232.
- (41) Schubauer, G. B.; Skramstad, H. K. Laminar Boundary-Layer Oscillations and Stability of Laminar Flow. *J. Aeronaut. Sci.* **1947**, *14*, 69–78.
- (42) Burns, M. A.; Johnson, B. N.; Brahmasandra, S. N.; Kalyan, H.; Webster James, R.; Madhavi, K.; Sammarco Timothy, S.; Man Piu, M.; Darren, J.; Dylan, H.; Mastrangelo Carlos, H.; Burke David, T. An Integrated Nanoliter DNA Analysis Device. *Science* **1998**, *282*, 484–487.
- (43) Figeys, D.; Pinto, D. Lab-on-a-Chip: A Revolution in Biological and Medical Sciences. *Anal. Chem.* **2000**, *72*, 330A–335A.
- (44) Paul, R.; Apel, J.; Klaus, S.; Schügner, F.; Schwindke, P.; Reul, H. Shear Stress Related Blood Damage in Laminar Couette Flow. *Artif. Organs* **2003**, *27*, 517–529.
- (45) Renault, C.; Li, X.; Fosdick, S. E.; Crooks, R. M. Hollow-Channel Paper Analytical Devices. *Anal. Chem.* **2013**, *85*, 7976–7979.
- (46) Masoodi, R.; Pillai, K. *Wicking in Porous Materials: Traditional and Modern Modeling Approaches*, 2012.
- (47) Thuo, M. M.; Martinez, R. V.; Lan, W.-J.; Liu, X.; Barber, J.; Atkinson, M. B. J.; Bandarage, D.; Bloch, J.-F.; Whitesides, G. M. Fabrication of Low-Cost Paper-Based Microfluidic Devices by Embossing or Cut-and-Stack Methods. *Chem. Mater.* **2014**, *26*, 4230–4237.
- (48) Suh, Y. K.; Kang, S. A Review on Mixing in Microfluidics. *Micromachines* **2010**, *1*, 82–111.
- (49) Glawdel, T.; Ren, C. L. Global Network Design for Robust Operation of Microfluidic Droplet Generators with Pressure-Driven Flow. *Microfluid. Nanofluid.* **2012**, *13*, 469–480.
- (50) Nisisako, T.; Torii, T.; Higuchi, T. Droplet Formation in a Microchannel Network. *Lab Chip* **2002**, *2*, 24–26.
- (51) Garstecki, P.; Fuerstman, J.; Stone, A.; Whitesides, M. Formation of Droplets and Bubbles in a Microfluidic T-Junction—Scaling and Mechanism of Break-Up. *Lab Chip* **2006**, *6*, 437–446.
- (52) Xu, J. H.; Li, S. W.; Tan, J.; Luo, G. S. Correlations of Droplet Formation in T-Junction Microfluidic Devices: From Squeezing to Dripping. *Microfluid. Nanofluid.* **2008**, *5*, 711–717.
- (53) Chen, Z.; Kheiri, S.; Young, E. W. K.; Kumacheva, E. Trends in Droplet Microfluidics: From Droplet Generation to Biomedical Applications. *Langmuir* **2022**, *38*, 6233–6248.
- (54) Chen, S. T.; Rong, W. M.; Shih, K. L.; Wang, N.; Tsai, C. Miniaturized Multiple Fourier-Horn Ultrasonic Droplet Generators for Biomedical Applications. *Lab Chip* **2010**, *10*, 2733–2740.
- (55) Lu, J.; Bu, R. F.; Sun, Z. L.; Lu, Q. S.; Jin, H.; Wang, Y.; Wang, S. H.; Li, L.; Xie, Z. L.; Yang, B. Q. Comparable Efficacy of Self-Monitoring of Quantitative Urine Glucose with Self-Monitoring of Blood Glucose on Glycaemic Control in Non-Insulin-Treated Type 2 Diabetes. *Diabetes Res. Clin. Pract.* **2011**, *93*, 179–186.
- (56) Mao, Y.; Tan, K. X. Q.; Seng, A.; Wong, P.; Toh, S.-A.; Cook, A. R. Stratification of Patients with Diabetes Using Continuous Glucose Monitoring Profiles and Machine Learning. *Health Data Sci.* **2022**, *2022*, 1.
- (57) Gainey Wilson, K.; Ovington, P.; Dean, D. A Low-Cost Inkjet-Printed Glucose Test Strip System for Resource-Poor Settings. *J. Diabetes Sci. Technol.* **2015**, *9*, 1275–1281.
- (58) Reach, G. Can Continuous Glucose Monitoring Be Used for the Treatment of Diabetes. *Anal. Chem.* **1992**, *64*, 381–386.
- (59) Zhu, W.-J.; Feng, D.-Q.; Chen, M.; Chen, Z.-D.; Zhu, R.; Fang, H.-L.; Wang, W. Bienzyme Colorimetric Detection of Glucose with Self-Calibration Based on Tree-Shaped Paper Strip. *Sens. Actuators, B* **2014**, *190*, 414–418.
- (60) MacDougall, D.; Crummett, W. B.; et al. Guidelines for Data Acquisition and Data Quality Evaluation in Environmental Chemistry. *Anal. Chem.* **1980**, *52*, 2242–2249.
- (61) Cai, L.; Wang, Y.; Wu, Y.; Xu, C.; Zhong, M.; Lai, H.; Huang, J. Fabrication of a Microfluidic Paper-Based Analytical Device by Silanization of Filter Cellulose Using a Paper Mask for Glucose Assay. *Analyst* **2014**, *139*, 4593–4598.
- (62) Zeng, S.; Baillargeat, D.; Ho, H.-P.; Yong, K.-T. Nanomaterials Enhanced Surface Plasmon Resonance for Biological and Chemical Sensing Applications. *Chem. Soc. Rev.* **2014**, *43*, 3426–3452.
- (63) Anker, J. N.; Hall, W. P.; Lyandres, O.; Shah, N. C.; Zhao, J.; Van Duyne, R. P. Biosensing with Plasmonic Nanosensors. In *Nanoscience and Technology*; Co-Published with Macmillan Publishers Ltd: UK, 2009; pp 308–319.
- (64) Wustholz, K. L.; Henry, A.-I.; McMahon, J. M.; Freeman, R. G.; Valley, N.; Piotti, M. E.; Natan, M. J.; Schatz, G. C.; Van Duyne, R. P. Structure–Activity Relationships in Gold Nanoparticle Dimers and Trimers for Surface-Enhanced Raman Spectroscopy. *J. Am. Chem. Soc.* **2010**, *132*, 10903–10910.
- (65) Cuiping, L.; Jiajie, L.; Shaozhen, L.; Huigao, D. Resonant Metasurfaces for Spectroscopic Detection: Physics and Biomedical Applications. *Adv. Dev. Instrum.* **2022**, *2022*, No. 9874607.
- (66) Wang, Y.; Zhang, X.; Wen, G.; Liang, A.; Jiang, Z. Facile Synthesis of a Highly SERS Active Nanosilver Sol Using Microwaves and Its Application in the Detection of *E. Coli* Using Victoria Blue B as a Molecular Probe. *Anal. Methods* **2016**, *8*, 4881–4887.
- (67) Wei, C.; Li, M.; Zhao, X. Surface-Enhanced Raman Scattering (SERS) With Silver Nano Substrates Synthesized by Microwave for Rapid Detection of Foodborne Pathogens. *Front. Microbiol.* **2018**, *9*, 2857.
- (68) Green, M.; Liu, F. M. SERS Substrates Fabricated by Island Lithography: The Silver/Pyridine System. *J. Phys. Chem. B* **2003**, *107*, 13015–13021.
- (69) Hakonen, A.; Svedendahl, M.; Ogier, R.; Yang, Z.-J.; Lodewijks, K.; Verre, R.; Shegai, T.; Andersson, P. O.; Käll, M. Dimer-on-Mirror SERS Substrates with Attogram Sensitivity Fabricated by Colloidal Lithography. *Nanoscale* **2015**, *7*, 9405–9410.
- (70) Saito, T.; Kimura, S.; Nishiyama, Y.; Isogai, A. Cellulose Nanofibers Prepared by TEMPO-Mediated Oxidation of Native Cellulose. *Biomacromolecules* **2007**, *8*, 2485–2491.
- (71) Song, J.; Birbach, N. L.; Hinestroza, J. P. Deposition of Silver Nanoparticles on Cellulosic Fibers via Stabilization of Carboxymethyl Groups. *Cellulose* **2012**, *19*, 411–424.
- (72) Li, D.; Li, D.-W.; Li, Y.; Fossey, S.; Long, Y.-T. Cyclic Electroplating and Stripping of Silver on Au@SiO₂ Core/Shell Nanoparticles for Sensitive and Recyclable Substrate of Surface-Enhanced Raman Scattering. *J. Mater. Chem.* **2010**, *20*, 3688–3693.
- (73) Pham, T. T. H.; Dac Dien, N.; Hoa Vu, X. Facile Synthesis of Silver/Gold Alloy Nanoparticles for Ultra-Sensitive Rhodamine B Detection. *RSC Adv.* **2021**, *11*, 21475–21488.
- (74) Sun, C. H.; Wang, M. L.; Feng, Q.; Liu, W.; Xu, C. X. Surface-enhanced Raman scattering (SERS) study on Rhodamine B adsorbed on different substrates. *Russ. J. Phys. Chem. A* **2015**, *89*, 291–296.
- (75) Koglin, E.; Kip, B. J.; Meier, R. J. Adsorption and Displacement of Melamine at the Ag/Electrolyte Interface Probed by Surface-Enhanced Raman Microprobe Spectroscopy. *J. Phys. Chem.* **1996**, *100*, 5078–5089.
- (76) Pu, H.; Xiao, W.; Sun, D.-W. SERS-Microfluidic Systems: A Potential Platform for Rapid Analysis of Food Contaminants. *Trends Food Sci. Technol.* **2017**, *70*, 114–126.
- (77) Kim, W.; Kim, Y.-H.; Park, H.-K.; Choi, S. Facile Fabrication of a Silver Nanoparticle Immersed, Surface-Enhanced Raman Scattering Imposed Paper Platform through Successive Ionic Layer Absorption and Reaction for On-Site Bioassays. *ACS Appl. Mater. Interfaces* **2015**, *7*, 27910–27917.
- (78) Li, X.; Liu, X. Fabrication of Three-Dimensional Microfluidic Channels in a Single Layer of Cellulose Paper. *Microfluid. Nanofluid.* **2014**, *16*, 819–827.
- (79) Zhao, C.; Thuo, M. M.; Liu, X. A Microfluidic Paper-Based Electrochemical Biosensor Array for Multiplexed Detection of Metabolic Biomarkers. *Sci. Technol. Adv. Mater.* **2013**, *14*, No. 054402.

- (80) Brooks, T.; Keevil, C. A Simple Artificial Urine for the Growth of Urinary Pathogens. *Lett. Appl. Microbiol.* **1997**, *24*, 203–206.